POLITECNICO DI TORINO
Repository ISTITUZIONALE

High rejection stacked single-layer graphene membranes for water treatment

Original
High rejection stacked single-layer graphene membranes for water treatment / Laurenti, M., Fontana, M., Raffone, F., Pellegrino, A., Bianco, S., Tresso, E., Pirri, C.F., Cicero, G.. - In: 2D MATERIALS. - ISSN 2053-1583. - 10:4(2023). [10.1088/2053-1583/ace45b]

Availability:
This version is available at: 11583/2980413 since: 2023-07-17T10:32:26Z

Publisher:
IOP Publishing

Published
DOI:10.1088/2053-1583/ace45b

Terms of use:

This article is made available under terms and conditions as specified in the corresponding bibliographic description in the repository

Publisher copyright

(Article begins on next page)

19 November 2026

2D Materials

PAPER • OPEN ACCESS

High rejection stacked single-layer graphene membranes for water treatment

To cite this article: Marco Laurenti *et al* 2023 *2D Mater.* **10** 045002

View the article online for updates and enhancements.

You may also like

- List of Participants
- Turbulence in two-dimensional forced electron-magnetohydrodynamics
A Celani, R Prandi and G Boffetta
- A provenance study on the lapis lazuli collection from the Regional Museum of Natural Sciences in Turin
L Guidorzi, A Re, D Angelici et al.

This content was downloaded from IP address 130.192.232.225 on 17/07/2023 at 10:54

2D Materials



OPEN ACCESS

RECEIVED
14 April 2023

REVISED
7 June 2023

ACCEPTED FOR PUBLICATION
5 July 2023

PUBLISHED
17 July 2023

Original content from this work may be used under the terms of the Creative Commons Attribution 4.0 licence.

Any further distribution of this work must maintain attribution to the author(s) and the title of the work, journal citation and DOI.



PAPER

High rejection stacked single-layer graphene membranes for water treatment

Marco Laurenti[1,2,*], **Marco Fontana**[1], **Federico Raffone**[2,*], **Alberta Pellegrino**[1], **Stefano Bianco**[1], **Elena Tresso**[1], **Candido F Pirri**[1,2] **and Giancarlo Cicero**[1]

[1] Department of Applied Science and Technology, Politecnico di Torino, Corso Duca degli Abruzzi, 24, 10129 Turin, Italy
[2] Center for Sustainable Future Technologies CSFT@Polito, Istituto Italiano di Tecnologia, Via Livorno, 60, 10144 Turin, Italy
[*] Authors to whom any correspondence should be addressed.

E-mail: marco.laurenti@polito.it and federico.raffone@iit.it

Keywords: graphene, nanopores, membranes, 2D material, water purification

Supplementary material for this article is available online

Abstract

Nowadays, the production of pure water from saltwater and wastewater is one of the most challenging issues. Polymeric materials represent, at the moment, the best solution for membranes technology but new materials with improved functionalities are desirable to overcome the typical limitations of polymers. In this work, graphene membranes with superior filtration properties are fabricated by stacking up to three graphene layers on a porous support and exploiting the intrinsic nanopores of graphene to filter diclofenac (drug), and methylene blue (dye). The rejection improves increasing the number of the stacked graphene layers, with the best results obtained with three graphene layers. Mass diffusion properties depend on the size of the probe molecule, consistently with the existence of intrinsic nanometer-sized pores within graphene. From the results of an in depth transmission electron microscopy analysis and molecular dynamics simulations it is inferred that graphene stacking results in a decrease of effective membrane pore sizes to about 13 Å diameter which corresponds to 97% rejection for diclofenac and methylene blue after one hour filtration.

1. Introduction

The supply of potable water and the environmental pollution from hazardous wastes are nowadays ones of the most challenging issues faced by the World. The resources of clean water currently available are constantly decreasing and the use of secondary water resources such as seawater and wastewater represents a powerful solution to make a huge amount of potable water available to meet the needs of the population. Seawater and wastewater require desalination and/or purification treatments to make the water drinkable. Therefore, the supply of clean water surely represents one of the most urgent critical issues of our days and both the problems of water desalination and wastewater treatment are of considerable attention.

In the last decades, membrane separation processes to purify water have replaced the most conventional ones such as distillation, sedimentation and adsorption. Separation membranes are widely accepted as the best existing technology for water treatment in terms of selective separation, cost-effectiveness, scalability, chemical and biological stability, and they have found numerous applications in water and dairy purification [1, 2], sea and brackish water desalination [3], energy harvesting [4], food and beverage production [5]. Nowadays, the filtration technologies commonly employed for desalination and wastewater treatment are typically based on the use of polymeric membranes operating in the micro and ultrafiltration regime [6]. Despite their widespread use, polymeric membranes suffer from low thermal, chemical and mechanical resistance, low flux, low separation factors, and considerable fouling phenomena that require high energy-consuming chemical washing operations, heavily reducing the membrane life cycle. Therefore, new-generation membrane materials are

© 2023 The Author(s). Published by IOP Publishing Ltd

highly desirable to improve the separation efficiency, enhance water permeability and reduce the energy consumption.

In the last years, the use of graphene in membrane technology [7, 8] started to be investigated thanks to its excellent mechanical strength and chemical stability provided by its peculiar crystal and chemical structure. The strength and stability of the σ bonds among C atoms make graphene a chemically-inert, lightweight material supposed to be the strongest material ever discovered in nature, about 200 times stronger than steel. Graphene is usually obtained by following top-down synthesis approaches, like mechanical and chemical exfoliation [9], or bottom-up synthesis methods, such as the epitaxial growth [10] and chemical vapor deposition (CVD) [11]. Among them, the CVD approach is one of the most investigated and it is already used for the large-scale production of high-quality graphene.

The first studies on the feasibility of graphene membranes for water treatment were based on molecular dynamic simulations [12, 13], which demonstrated that nanoporous single-layer graphene (SLG) could withstand strong pressure regimes (up to 57 MPa) and allow ultra-fast water permeability, due to its atomic thickness. Additionally, high salt rejection was predicted if the presence of nanopores with ad hoc size, density and chemistry is induced within the graphene layer structure. Given the chemical stability of graphene, the material is less prone to be attacked by foulant. Additionally, the hydrophobic nature of graphene [14, 15] can be exploited to build amphiphilic composites that are particularly effective against fouling [16].

The molecular and ionic transport properties across SLG membranes was then evaluated experimentally. SLG was transferred on various porous supports such as polymeric membranes [17, 18], metal grids and SiN/Si with an array of holes [19–22]. By taking advantage of intrinsic defects within the SLG as single holes, wrinkles and tears, the selective transport of molecules with different size (NaCl, KCl, tetramethylammonium chloride, Allura red dye and tetramethylrhodamine dextran) across the graphene membrane was studied and the rejection ability of the graphene intrinsic defects demonstrated. To further improve the separation efficiency, several technological approaches were investigated to introduce subnanometer-sized pores of different but uniform size within the graphene active layer. Some of them include a multistep approach based on interfacial polymerization (to seal large defects) and atomic layer deposition to fill nanometer-sized defects [18], O_2 plasma etching [21, 22] or the combination of Ga^+ ions bombardment and the subsequent enlargement of the ion-induced defects by oxidative etching [23]. Overall, these approaches were found to be effective for membranes suitable for the early stages of filtration where molecules larger than monatomic ions are rejected. They, however, failed in providing membranes for desalination given the large size of pores (>5.5 Å of diameter) [12].

Even though different methods have already been reported for the fabrication of SLG membranes and satisfactory results in terms of water desalination and selective transport of molecules have been achieved, most of them have been accomplished at a very small scale, often involving the use of graphene membranes obtained by quite sophisticated fabrication processes and with a limited active area (from few μm^2 to few cm^2). These aspects highly limit the large-scale use and production of graphene membranes. Therefore, simple, fast and low-costs methods to develop SLG membranes are needed. Beside graphene, other carbon-based materials have been used to treat wastewater. Graphene oxide (GO) nanosheets allow for water filtration thanks to the presence of functional groups and small interlayer distances that effectively block the solute particles. The presence of functional groups and small distances between layers contributes in the rejection of the solute [24]. However, unlike graphene, GO is structurally less resistant and more prone to mechanical breaking due to high pressure and to chemical attack [25]. GO can also be used as precursor for the creation of graphene membranes with controlled pore distributions [26, 27]. Other possibilities involve carbon nanotubes that show high water transport. However, limitations are due to the difficulty in reliably fabricating sub-nanometer sized tubes [28].

This work deals with the fabrication of stacked SLG membranes for nanofiltration obtained by the multiple transfer of SLG having nanometer-sized intrinsic porosity, on PolyCarbonate Track-Etched (PCTE) porous supports. The choice of graphene is due to its selectivity, mechanical strength, resistance to fouling, and its affinity with the materials used for support. A simple, fast and repeatable direct transfer method was developed to transfer SLG from the starting copper foil to PCTE. In this study we considered membranes obtained by stacking up to three layers graphene, but the process could be repeated to obtain thicker membranes, if needed. The coverage of PCTE with graphene and the presence/typology of graphene defects (single holes, wrinkles and tears) were studied by electron microscopy and correlated to the number of stacked graphene layers. Raman spectroscopy and x-ray photoelectron spectroscopy (XPS) were also carried out to investigate the structure and surface chemistry of the stacked SLG membranes. Finally, the mass transport across the as-prepared membranes was evaluated in a side-by-side diffusion cell, by considering solute molecules of different size: NaCl, diclofenac (DF) in sodium salts form, and methylene blue (MB) organic dye. The rejection results, also corroborated by numerical computation

results, are discussed in terms of molecule size, number of the stacked graphene layers and presence of intrinsic nanometer-sized pores within the graphene structure.

2. Results and discussion

2.1. Morphology, structure and surface chemistry of stacked graphene-based membranes

The surface morphology of the membranes was investigated by means of field-emission scanning electron microscopy (FESEM) analysis. Figure 1(a) shows the surface of the PCTE support alone, with 100 nm open pores distributed on the whole sample surface, a size comparable with the size of the pores of currently manufactured graphene membranes [29]. Figures 1(b)–(d) show the surface of the stacked SLG membranes after the transfer of one (b), two (c) and three (d) layers of graphene on PCTE, according to the transfer method described in section 4.1. The presence of graphene, even suspended over the pores of the underlying PCTE substrate, is clearly visible as represented by the presence of wrinkles typically observed when graphene is transferred onto various kinds of supports [30, 31]. The bright spots indicate the presence of some contaminants formed during the Cu etching process, which appear in the form of iron oxide nanoparticles, as confirmed by XPS data discussed in the following. If the low-magnification images of the different samples are considered (figure 2), it can be observed how the PCTE coverage improves by increasing the number of the stacked graphene layers. The defectiveness affecting the graphene membranes, expressed in terms of uncovered PCTE regions/pores and of tears due to the rupture of graphene suspended over the pores, is minimized in the case of sample PCTE/TLG (three stacked graphene layers, figure 2(c)), while it is still pronounced for samples PCTE/SLG (single graphene layer, figure 2(a)) and PCTE/DLG (two stacked graphene layers, figure 2(b)). The coverage of the PCTE support due to the transfer of graphene and the quality of the final graphene-based membrane is then optimized and maximized after stacking three graphene layers. In facts, unlike previously reported stacked membranes where rejection occurs at the intersections between partially overlapped graphene layers [32], here the filtration mechanism is based on the size of the pores located in the graphene sheets.

Raman spectra directly acquired on the PCTE/SLG, PCTE/DLG and PCTE/TLG membranes confirm the findings from SEM analyses. On PCTE/SLG, Raman analysis evidences the presence of uncovered PCTE areas (figure 3), while on PCTE/DLG and PCTE/TLG the coverage is uniform. In the covered areas, Raman peaks related to the G band at $\sim$1580 cm^{-1} and 2D band at $\sim$2700 cm^{-1} are detected (figures 3 and 4). In particular, the G peak is partially overlapped with one of the main peaks of PCTE positioned at $\sim$1600 cm^{-1}, but it emerges evidently through a deconvolution process, as shown in figure 4. No noticeable difference is highlighted in the Raman analysis between PCTE/SLG, PCTE/DLG and PCTE/TLG. In fact, differences in the Raman profile are reported as the number of layers of graphene transferred on SiO_2 increases, but such differences cannot be revealed when the substrate is PCTE. It is remarkable to point out that in no case the D peak at $\sim$1350 cm^{-1} is observed, giving evidence of the limited defectiveness induced during the transfer process.

Further insight into the morphology and structure of the single layer graphene membrane is obtained by transmission electron microscopy (TEM), which allows for the investigation of porosity at the nanometer scale. Figure 5 provides a representative analysis of a single layer region, as confirmed by imaging the edge of the suspended graphene membrane (figure 5(a)). Since the transfer method used for TEM sample preparation is the same as for the PCTE/graphene membranes, high magnification TEM images (figure 5(b)) are a valuable tool for direct visualization of the intrinsic nanometer-sized porosity of the membrane.

Before discussing these results, few comments must be made on the interaction of the electron beam with single layer graphene and its influence on pores through knock-on damage and chemical effects. Based on the existing literature [33], 80 keV electrons do not produce holes in defect-free regions of single layer graphene through knock-on damage. However, if holes are already present in the membrane, it is possible to enlarge the holes with 80 keV electrons as a function of dose since the knock-on damage threshold for carbon atoms at the edges is lower ($\sim$50 keV) [34]. Another effect that must be considered is the production of extended holes even at low energies ($\sim$20 keV) [33] in regions with extended hydrocarbon contamination. Given all the aforementioned considerations, high-magnification TEM images were acquired in this study by minimizing the electron dose on regions where the hydrocarbon contamination (dark features in figure 5(b)) is relatively low. Holes are clearly visible in TEM images, with areas in the range 40 $\div$ 250 Å^2, as measured with the specific ImageJ selection tool. Based on the initial discussion on the electron-beam interaction with graphene, there is a possibility that these values are slightly overestimated. However, it must be stressed that 80 keV electrons can predominantly produce holes only in regions where porosity is already present. Therefore, TEM images provide proof of the existence of such porosity in the membrane. Moreover, it must be noted that the estimated values for the area of the pores are approximately in accordance with the interpretation of

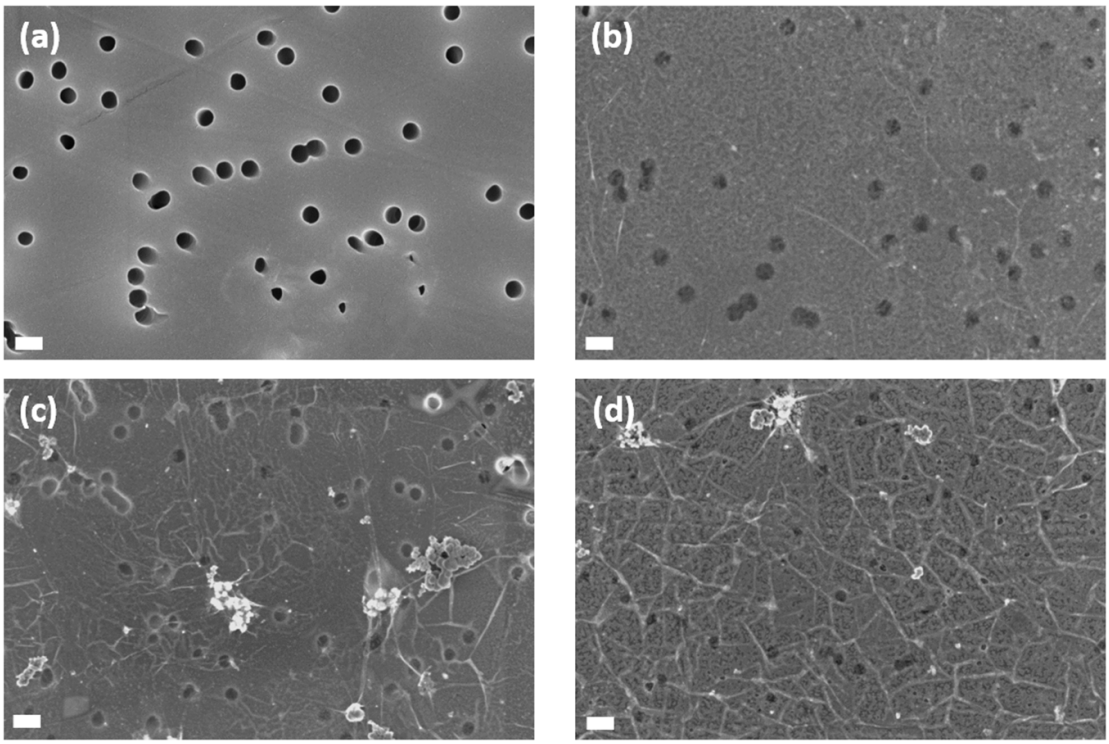


Figure 1. FESEM images of (a) PCTE and (b)–(d) PCTE/graphene membranes prepared by stacking different number of graphene layers: (b) single layer, (c) two layers, and (d) three layers. Scale bar is 200 nm.

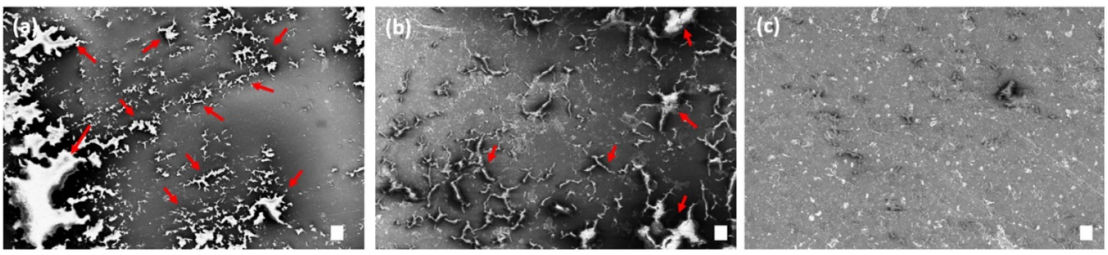


Figure 2. FESEM images of (a) PCTE/SLG, (b) PCTE/DLG, and (c) PCTE/TLG membranes. Red arrows indicate PCTE regions uncovered by graphene, showing the typical charging effects induced by the electron beam. Scale bar is 2 μm.

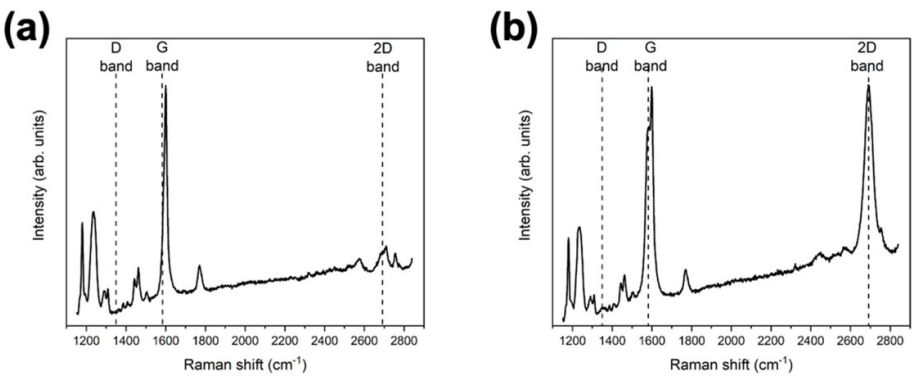


Figure 3. Raman spectra acquired on PCTE membrane after the transfer of a single layer of graphene. The co-presence of uncovered PCTE regions is confirmed by Raman spectroscopy (a). Nonetheless, the successful transfer of graphene over PCTE is confirmed (b).

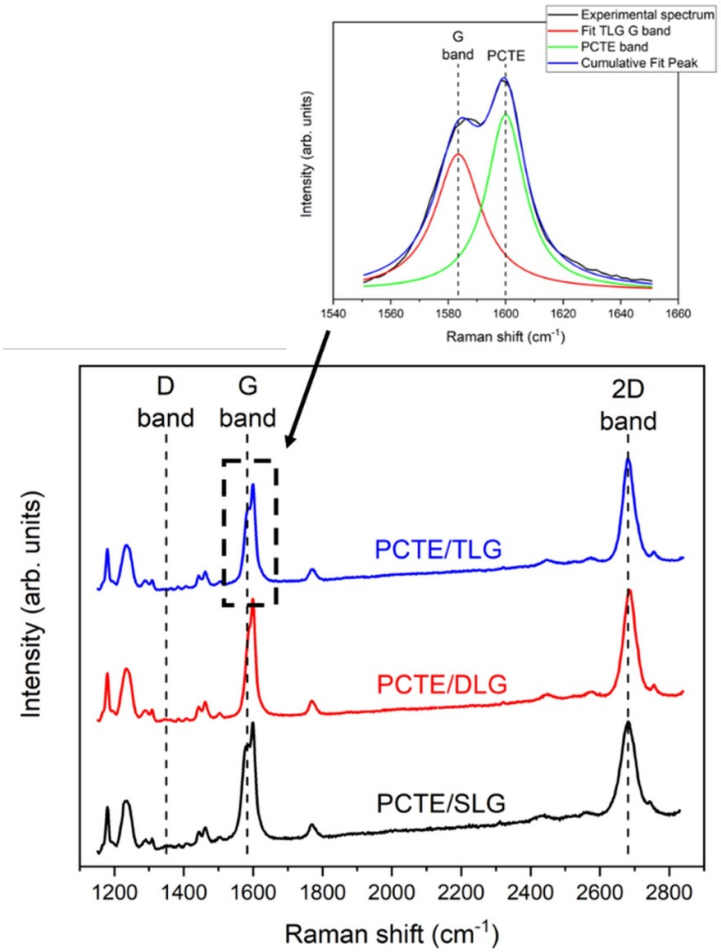


Figure 4. Raman spectra acquired on the stacked single-layer graphene membranes over PCTE supports. The inset shows the partial overlap affecting G peaks of graphene and PCTE.

mass transport diffusion and the classical molecular dynamics simulations reported in the following sections of the manuscript.

XPS study was performed to investigate the surface chemistry of the membranes. Figure S2 of the S.I. shows the wide-scan energy XPS spectra collected for bare PCTE (panel a) and for the stacked graphene membranes (panels b-d). In the case of bare PCTE, only C (83.8 $\pm$ 0.4 At. %) and O (16.2 $\pm$ 0.4 At. %) elements were detected, as expected. For PCTE/graphene membranes, other elements like Si ($\leqslant$1 At. %) and Fe (1.5–7 At. %) were found as contaminants due to the membrane fabrication process, that involves a chemical etching step in iron chloride bath to remove the Cu foil and transfer the graphene layer over the PCTE support. In particular, iron oxide-based precipitates in the form of nanoparticles can be inferred from FESEM results discussed previously and by considering the presence of components associated to iron oxide-related species after deconvolution of core-level O 1 s spectra shown in figure S3 of the S.I.

More insight about the surface chemistry of the stacked SLG membranes was obtained by collecting core-level C 1s XPS spectra. For bare PCTE (figure 6(a)), deconvolution of the corresponding C 1s peak was performed according to [35]. Two main components positioned at 284.8 eV and 285.2 eV are due to C–C and C–H bonds, respectively. A secondary component due to C–O–C is positioned at 286.7 eV. An additional peak due to O–C=O and a shake-up are also present in the higher BE region (289–292 eV). The presence of graphene in the PCTE/graphene membranes is clearly highlighted by the rise of a distinct C–C component positioned at 284.5 eV and due to atoms arranged in the graphitic-like structure (figures 6(b)–(d)). This peak is well-resolved with respect to the one associated to C–C arranged in the polymer chain of the underlying PCTE membrane support (284.8 eV). The percentage area of the C–C component due to graphene increases according to the number of the stacked graphene layers, changing from 22% for a single layer up to 28% for three layers of graphene. In this last case, a distinct shake-up peak positioned at about 290 eV and due to π-π^* interlayer interactions among the stacked graphene layers [36] is observable and is a further evidence of the stacked structure for the graphene membranes considered in this work. The deconvolution of high-resolution (HR) C 1s spectra

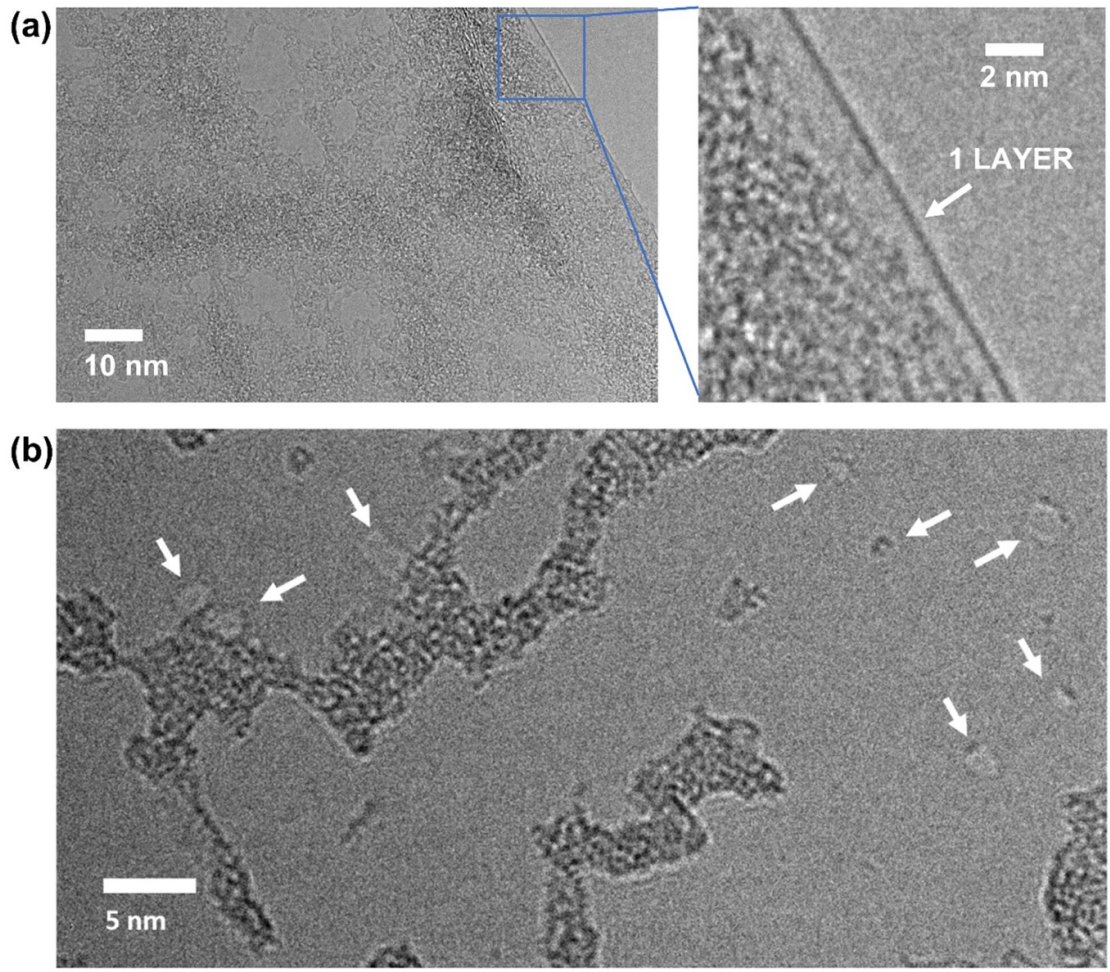


Figure 5. Bright-field TEM image of a single layer graphene region (a), alongside a high magnification TEM image showing nanometer-sized porosity (pointed by arrows) (b).

for samples PCTE/DLG and PCTE/TLG also evidences the presence of an additional component positioned at about 283.4 eV, which is generally ascribed to metal carbides. However, the presence of these chemical species can be excluded in this work. On the other hand, according to other literature works, this additional component is associated with the presence of defects in the graphitic structure [37–39]. According to Raman and TEM results discussed previously, the origin of this peak is most likely due to the intrinsic defectiveness of graphene, including nanopores, rather than to the defects induced by the transfer process.

2.2. Classical molecular dynamic simulations

For graphene-based membranes the principal filtration mechanism is steric hindrance. Estimating the size of the molecules to be filtrated can give an insight into the pore size limit that the membrane has to show for an effective separation. The exact volume occupied by a solute molecule cannot be determined *a priori* as it highly depends on its hydrophilic, hydrophobic, or amphiphilic character and the nature of the atoms constituting its functional groups. Atomistic simulations, able to describe the details of the interatomic interaction, are therefore needed to achieve such a task [40]. To quantify the volume occupied by a molecule, it is necessary to determine both the Pauli repulsion length of each atom constituting the solute molecule and the shape of the solvation shell around it.

To identify the occupied volume of the two probe molecules considered in this work, DF and MB, we assigned to each atom of these molecules a spherical volume. Within such spherical volumes, interactions with other atoms (for instance the ones belonging to a membrane pore) are repulsive. For the determination of each atom's sphere radius, we performed a set of classical molecular dynamics simulations where the two molecules were immersed in a bulk of water. For each atom we identified the distribution of both water's hydrogen and oxygen as function of the distance from the probe molecule's atom (see supporting information for a selection of distributions). In such distributions the distance of the first peak, identifying the location of the nearest water

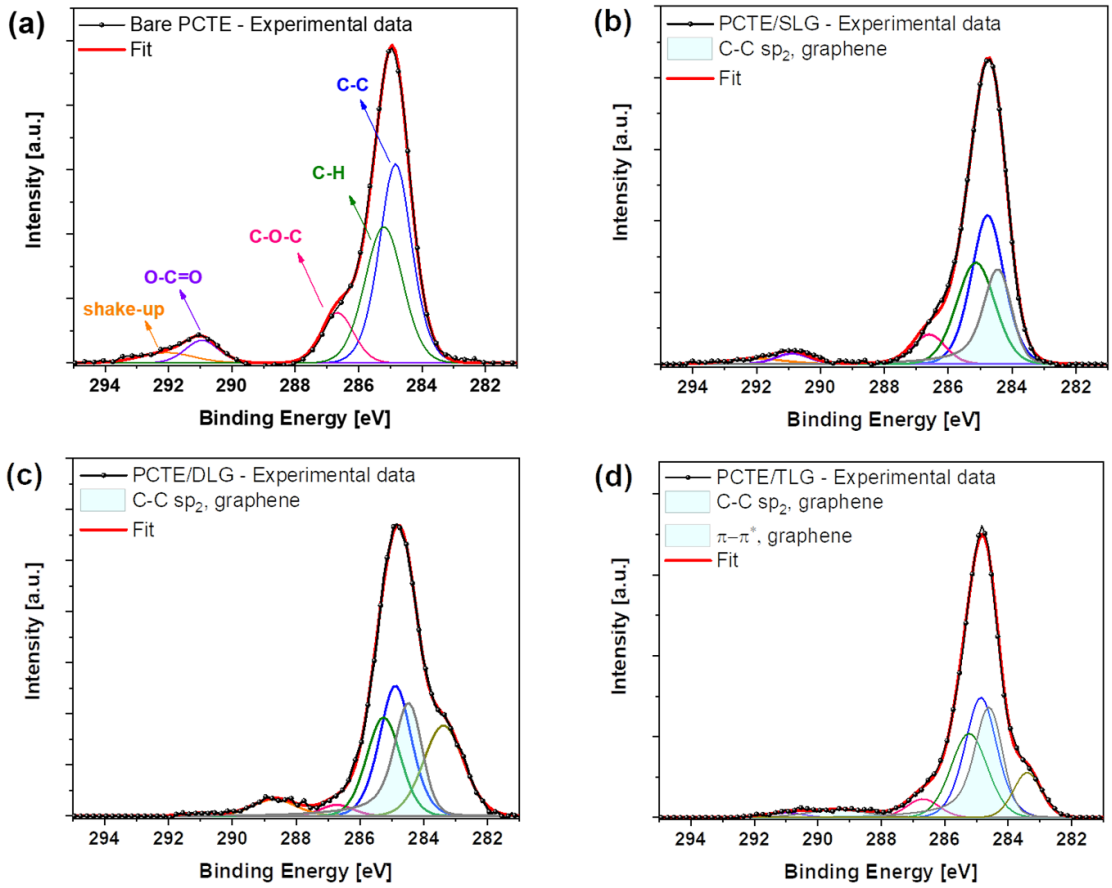


Figure 6. Core-level C 1s XPS spectra collected for (a) bare PCTE, (b) PCTE/SLG, (c) PCTE/DLG, and (d) PCTE/TLG. Filled-area components represent the contribution coming from the presence of graphene. Colored lines represent the components for bare PCTE substrate.

molecule, was considered the maximum space occupied by the inspected atom and it was taken as radius of the sphere. Figures 7(a) and (b) show the structure of the two probe molecules while figures 7(c) and (d) the related occupied space calculated as described.

As explained previously, the probe molecule steric hindrance is not only to be attributed to the volume occupied by each atom of the molecule. Much of the overall occupied volume of the test molecule is determined by its solvation shell. Unlike simpler salts like Na^+/Cl^-, where the shell covers completely the atom, for extended molecules like DF or MB the identification of the solvated regions is more complex. Different parts of the molecule can show a more hydrophilic or hydrophobic character depending on the exposed functional groups. To define whether or not water can be considered as part of the solvation shell, we performed a set of geometry relaxation calculations for a system comprising of the probe molecule and a single H_2O for different adsorption sites. For each arrangement the binding energy (BE) was calculated. Results are summarized in table 1. Concerning DF, the strongest bond is found when a water molecule interacts with the oxygen of the CO_2^- group (labeled as site I in figure 7(a)). The BE in this case (−0.51 eV) is comparable with the energy of a hydrogen bond between two water molecules (−0.53 eV). Such a strong interaction can be explained in terms of charge distribution. The anion negative charge is mostly localized on the oxygen of the CO_2^- group (−0.83 |e| according to the local charges) which attracts the hydrogen of water. As a result of the intense bond, the effective occupied volume by the molecule next to the CO_2^- group must include the first solvation shell, with consequences on its permeability through the membranes. It is unlikely for DF to release the H_2O molecule when passing through a pore. The remaining part of the molecule only weakly interacts with the surrounding water given the high hydrophobic character of the two benzene rings and their terminations. A water molecule adsorbed next to a ring (labeled as site II in figure 7(a)) leads to a BE of only −0.11 eV. In this case interactions are mainly driven by van der Waals forces. The distribution of water around DF confirms the different nature of the bonds (see supporting information). The water distribution around the oxygen of the CO_2^- group is sharply peaked signifying a strong H-bond, whereas around a hydrogen or a chlorine atom belonging to the benzene ring the distribution is much broader.

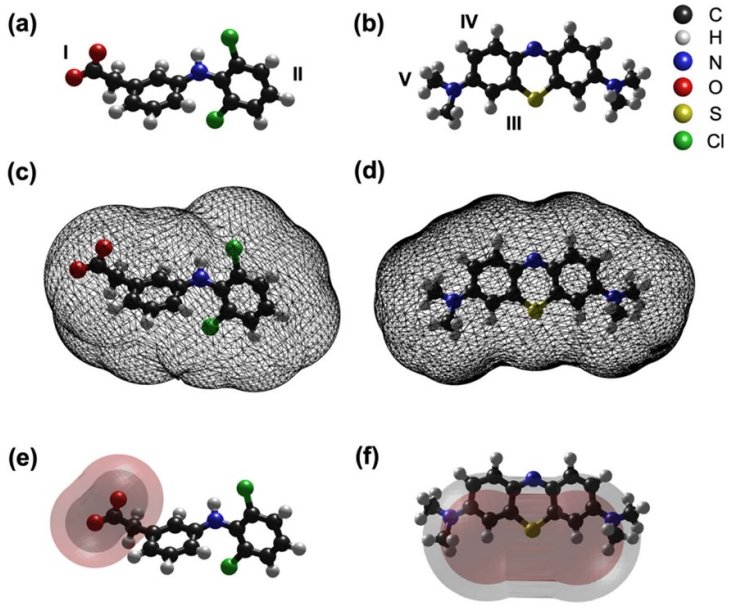


Figure 7. Diclofenac and methylene blue structure ((a) and (b)). Roman numbers indicate water adsorption sites specified in table 1. Space occupied by the atoms of the two molecules ((c) and (d)). Location of the first solvation shell ((e) and (f)). The position of hydrogen is depicted in grey while the one of the oxygen in red. The portions of the solvation shell clipping into the molecule are just for illustrative purposes and they are not to be considered indicative of the water molecule locations.

Table 1. Binding energies of notable interactions between water, diclofenac and methylene blue. Energies are reported in eV. The site label indicates a bond between a water molecule and the respective atoms indicated in figures 7(a) and (b).

Involved molecules	Binding energy (eV)
H_2O—H_2O	−0.53
Diclofenac—H_2O (site I)	−0.51
Diclofenac—H_2O (site II)	−0.11
Methylene blue—H_2O (site III)	−0.39
Methylene blue—H_2O (site IV)	−0.17
Methylene blue—H_2O (site V)	−0.17

For MB, site III where water interacts with the hydrogen atoms next to the positively charged sulfur leads to a BE of −0.39 eV, which is minor in intensity, but still comparable, with DF's O-water interaction strength. The other sites, IV and V, respectively a hydrogen next to nitrogen and a hydrogen belonging to the methyl group show smaller interaction energies (−0.17 eV). Compared to DF, MB has a slightly more homogeneous character although we can still say that the solvation shell is likely to form only in a specific region of the molecule, namely the area next to sulfur.

Based on the previous analyses, we extended the occupied volume of the probe molecules considering the presence of water in the previously identified region. A depiction of the location of the first shell of water for both probe molecules can be found in figures 7(e) and (f). We assumed that the spatial occupation of a water molecule in the solvation shell corresponds to the sigma parameter of the Lennard–Jones potential used to describe it (3.16 Å). Given these assumptions, we calculated the smallest section of occupied by each molecule as an indication of the limit size of the membrane pores. For DF, we obtained a minimal section of 125.4 $Å^2$ roughly corresponding to a circular pore with a diameter of 12.6 Å. For MB, the resulting minimal section is 123.1 $Å^2$ which corresponds to a 12.5 Å diameter pore. The similar effective section of the two test molecules agrees with the analogous rejection performances measured experimentally in the case of TLG, as discussed in the next section 2.3. In the case of NaCl, it is well established in literature a limit pore size of 5.5 Å [12, 27].

2.3. Analysis of mass transport diffusion across graphene-based membranes

The mass diffusion across graphene covered PCTE membranes was evaluated by considering the diffusion of NaCl, DF and MB as probe molecules in a forward osmosis test cell. During the experiment one compartment of the test cell is filled with distilled water while the other is filled with a solution containing NaCl, DF or MB (feed solution). The two compartments are separated by the membrane: PCTE or PCTE covered with graphene. During the forward osmosis experiment, the concentration of the solute in the compartment initially containing pure water (permeate side) is analyzed at different times. The mass transport through the membrane is characterized in terms of a parameter R defined as $R(t) = \left(1 - \frac{C(t)}{C_0}\right) \times 100$, where C_0 is the initial concentration in the feed solution and $C(t)$ the concentration of the permeate solution evaluated

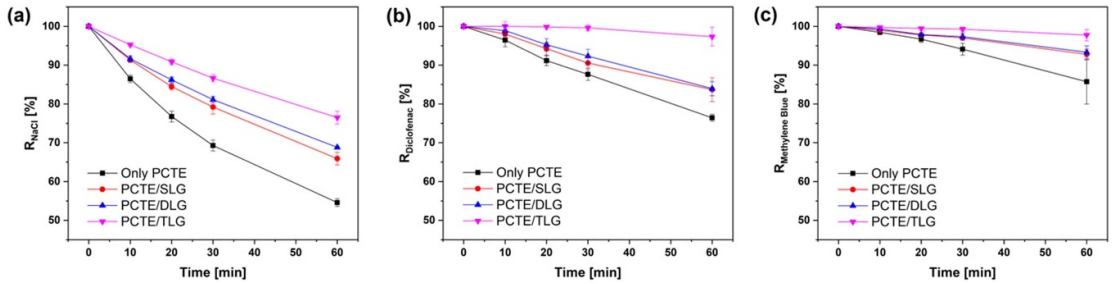


Figure 8. *R* parameter for NaCl (a), diclofenac (b), and methylene blue (c) measured for bare PCTE and graphene-based PCTE membranes made of single graphene layer (PCTE/SLG), two (PCTE/DLG) and three (PCTE/TLG) graphene layers.

after specific time intervals (0 min, 10 min, 20 min, 30 min, 60 min). The *R* parameter represents the percentage of particles retained in the feed region after a given time *t*. NaCl, given its reduced dimensions, is considered a control probe, providing base indications on the flux through the membrane for a solute which is not blocked by the membrane (see figure 8(a)). Intrinsic defects in graphene larger than 1 nm are, indeed, present, as estimated by TEM analyses, allowing for the passage of NaCl. In figure 8(a) it is clear that for NaCl, as the number of graphene layers increases, the slope of the *R* parameter as a function of time increases. In particular, the *R* parameter after 60 min increases from 55%, for only PCTE, to 67% with a single layer of graphene transferred atop the PCTE support. By further increasing the number of the stacked graphene layers, the *R* parameter increased accordingly, approaching 77% when three layers of graphene were stacked on each other (sample PCTE/TLG). The presence of more layers has then an impact on the amount NaCl that permeates through the membrane. By comparing the *R* parameter slope of NaCl with the one of the larger DF and MB molecules, the selectivity of the different membranes can be inferred. As shown in figures 8(b) and (c), DF and MB *R* parameters are significantly flatter over time. In the case of DF, the bare PCTE alone was able to block 76% of the drug in an hour. If the graphene-based membranes are considered, the drug selectivity was further improved and it changed from around 84% for both PCTE/SLG and PCTE/DLG, up to 97% in the case of sample PCTE/TLG. Similarly, MB *R* parameter was found to be around 86% for PCTE only. The addition of graphene to PCTE allowed to promote the selectivity of the dye, approaching 98% by stacking three graphene layers. More generally, it can be observed that the *R* parameter increases by increasing the number of the stacked graphene layers, with the best rejection results achieved with sample PCTE/TLG (three graphene layers). The investigated TLG membranes show very promising rejection properties if the average size of the probe molecule is higher than 1 nm, i.e. DF and MB.

The filtration results shown in figure 8 can be explained by first considering the existence of extended defects due to the fabrication process of the membrane. FESEM analyses pointed out the presence of uncovered regions of PCTE after the transfer of a single layer of graphene as well as of tears in the graphene layer. Then, the degree of PCTE coverage can be maximized by stacking more than one graphene layer and the filtration properties of the stacked graphene membranes improve accordingly. On the other side, a clear dependence of the filtration properties on the size of the molecule was observed for all the graphene-based membranes analyzed in this work and suggests the existence of an intrinsic porosity in the graphene layer structure. In particular, nanopores featuring an average pore size comparable to that of Na^+ and Cl^- ions can be expected, since these ions are able to diffuse across the PCTE/graphene membranes, even in the case of the highest number of stacked graphene layers (sample PCTE/TLG). On the other hand, both MB and DF (whose average size is higher than 1 nm, as previously discussed) are successfully rejected from the graphene membranes. In particular, an almost complete blockage of these molecules (approaching 100%) was found by stacking three layers of graphene. Therefore, it can be concluded that most of the intrinsic pores within the graphene structure have an average size comparable or higher than salt ions ones. The passage of water molecules and Na^+/Cl^- ions is then allowed, while bigger molecules like MB and DF are completely rejected. TEM analysis estimated an intrinsic defective pore size in the range 40–250 $Å^2$, which implies that an SLG/PCTE membrane cannot selectively block solute with size smaller than this pore dimensions. Indeed, all tested solutes show poor rejection when an SLG/PCTE is used since the largest solutes considered in this work DF and MB, have an estimated size of 125 $Å^2$. When two or three single layer graphene are overimposed, statistically open pores of the first layer are covered by pristine graphene areas of the second or third layer, thus the membranes show high selectivity for larger molecules. NaCl still percolated through

the TLG/PCTE membrane pores and its blockage remains poor. We did not study thicker multi-layer membranes (with number of graphene layers $\geqslant 4$) since the three-layer system already proved the principle that layer stacking is an effective way to patch extended intrinsic defects in graphene and to increase selectivity.

3. Conclusions

Stacked graphene-based membranes were obtained by the transfer of one, two or three SLG on a porous PCTE support. Electron microscopy, Raman and XPS analyses revealed that extended defects affecting the graphene-based membranes such as uncovered PCTE regions or graphene holes, tears and wrinkles, could be minimized by stacking up to three layers of graphene. This aspect turned out into improved filtration properties. Indeed, by increasing the number of stacked graphene layers, the selectivity toward drug and dye molecules could be maximized when three layers of graphene were stacked on the PCTE support. On the other side, the salt was still passing through the membrane because of the existence of few-nanometer scale defects in the graphene lattice structure with a limit pore size comparable to the dimension of DF and MB, which could not be completely sealed by stacking an increasing number of graphene layers. The presence of such intrinsic nanometer-sized pores in the graphene structure is supported by TEM. Atomistic simulations allowed to evaluate the steric hindrance of the probe molecules. It was found that the effective sections of DF (125.4 $Å^2$) and MB (123.1 $Å^2$) are similar and larger than that of NaCl, for which a limit pore size is required (5.5 Å). These findings justify the similar but superior selectivity measured for DF and MB especially in the case of the three-layer graphene structure. Moreover, they further corroborate the conclusion that graphene intrinsic nanopores with a limit pore size comparable to the effective section of DF and MB molecules are present.

4. Methods

4.1. Fabrication of stacked SLG membranes

Hydrophobic PVP-free track-etched polycarbonate membranes (PCTE, 25 mm diameter, 100 nm average pore size) were purchased from Sterlitech Corporation (USA). SLG grown on copper (Cu) foil by CVD was purchased from Graphenea (Spain) and used as received.

SLG was transferred from the Cu foil on the porous PCTE membranes with a direct transfer procedure, consisting of the following steps: (i) the PCTE membrane was placed atop of the SLG/Cu sample, in direct contact with the graphene surface; (ii) the overall PCTE/SLG/Cu sample was transferred to a 1.5 M $FeCl_3$ solution and let floating over the etching bath for 30 min until the complete removal of the Cu foil. At the end of the Cu etching, the single layer of graphene completely adhered to the PCTE membrane. Adhesion of graphene on PTCE takes advantage of the hydrophobicity of the polymer so no pressure is required during the process unlike similar fabrication procedures reported in literature [41]. (iii) the PCTE/SLG membrane was washed three times in de-ionized water (10 min each time) to remove contaminants of the etching solution as much as possible; (iv) the PCTE/SLG membrane was finally air-dried.

Stacked SLG membranes consisting of two (PCTE/DLG) and three (PCTE/TLG) layers of graphene were fabricated by repeating the procedure described above. At the beginning of the transfer process, the SLG/Cu sample was placed atop of a PCTE/SLG or PCTE/DLG membrane, respectively for preparing PCTE/DLG and PCTE/TLG. More generally, the method herein proposed can be repeated every time an additional layer of graphene has to be stacked.

4.2. Characterization techniques

FESEM of bare PCTE and PCTE/Graphene membranes was carried out with a SUPRA™ 40 microscope (Zeiss). FESEM images were acquired at an acceleration voltage of 1.2 kV. The PCTE/Graphene membranes were not metal coated, in order to maximize surface contrast between graphene-covered regions and bare PCTE. TEM on single layer graphene was carried out with an FEI Tecnai G2 F20 S-twin electron microscope, operating at 80 kV to minimize knock-on damage [33]. Image processing and analysis were performed with Gatan Microscopy Suite and ImageJ software. Concerning sample preparation, commercial single layer graphene was transferred onto the lacey carbon side of Au TEM grids using a direct transfer technique comparable to the one described in section 4.1. Micro-RAMAN spectroscopy was performed by using a Renishaw InVia Qontor Raman microscope. A laser diode source ($\lambda = 532$ nm) was used with 5 mW power, and sample inspection occurred through a microscope objective (50X), with a backscattering light collection setup. XPS was carried out by using a PHI 5000 VersaProbe (Physical Electronics) system. The x-ray source is monochromatic Al Kα radiation (1486.6 eV). Wide-energy and high-resolution XPS spectra were analyzed using CasaXPS software (version 2.3.18). All the XPS spectra were processed after Tougaard background subtraction [42]. HR C 1s core level spectra deconvolution into individual mixed Gaussian–Lorentzian peaks was obtained after BE calibration according to C 1s position for adventitious carbon (284.8 eV).

4.3. Analysis of diffusion transport properties

The diffusion transport properties across PCTE/graphene membranes were analyzed in a side-by-side diffusion glass cell (Permegear Inc., USA). For each measurement a new membrane was fabricated and tested. The side-by-side system is made of two glass cells (5 ml volume) and a clamping system to connect each other by an orifice (15 mm diameter). The mass transport measurements were carried out by clamping the membrane between the two chambers, by using three different aqueous solutions: NaCl, DF (a nonsteroidal anti-inflammatory drug) and MB (an organic dye). About 1.461 g NaCl (from Sigma) was dissolved in 50 ml of de-ionized water. About 0.159 g DF (from Sigma, in sodium salt form) was dissolved in bidistilled water under vigorous magnetic stirring for 30 min at room temperature. About 0.1 mM MB solution was prepared starting from 3.6 mM commercial MB solution (from Sigma). The left chamber was filled with 5 ml NaCl, DF or MB solution (feed solution) and the right chamber with 5 ml de-ionized water (permeate solution). The active side of the membrane (i.e. the one covered with graphene) faced the left chamber (feed solution). Both solutions were maintained under magnetic stirring for the overall time of the experiment in order to minimize concentration polarization effects. To avoid cross-contamination issues, each glass cell was cleaned five times with ethanol at the end of each filtration experiment.

The mass transport properties of the membranes were defined in terms of R parameter (%), according to the following equation:

$$\mathrm{R}\ (\%) = \left(1 - \frac{C(t)}{C_0}\right) \times 100$$

with C_0 being the starting concentration of the feed solution and $C(t)$ the concentration of the permeate solution evaluated after specific time periods (0 min, 10 min, 20 min, 30 min, 60 min). NaCl and DF concentration was evaluated by measuring the permeate solution conductivity at different times using a Pt conductivity electrode probe (AMEL Electrochemistry). Conductivity was recorded every 20 s for 60 min with a multi-channel potentiostat (Arbin Instruments) connected to the probe and using NOVA Autolab software. NaCl and DF concentration values were then obtained starting from a calibration curve. MB concentration was obtained by UV–vis spectroscopy. About 100 μL was withdrawn from the permeate solution at specific times (0 min, 10 min, 20 min, 30 min, 60 min) and the corresponding UV absorbance spectra (figure S1 of the supporting information, S.I.) acquired with a Multiskan go microplate reader (ThermoScientific). The MB concentration was then estimated from a calibration curve, by considering the characteristic MB UV absorbance at $\lambda = 663$ nm. The data on concentration of NaCl and DF from the Pt conductivity measure and on MB from the UV–vis spectroscopy were then collected together and plotted in figure 8 at 0, 10, 20, 30 and 60 min to allow for direct comparison among the curves.

4.4. Simulation methodology

Classical molecular dynamics simulations were carried out with LAMMPS [43, 44]. The dynamics consisted of a bulk of 1800 water molecules and dissolved Na^+/DF or MB/Cl^- couples. The simulation was carried out in an NPT ensemble at 300 K and 1 atm, maintained with a Nosé–Hoover thermostat and barostat, for 1 ns with a timestep of 1 fs. The water distribution around the organic solutes was calculated every picosecond and mediated over the entire duration of the dynamics. Water potential was described with TIP4P force field [45] while the ionic organic molecules were described with GAFF2 force field [46]. In order to assign electrostatic point charges to each atom of the molecules, we performed Hartree–Fock (HF) calculations using a 6–31G(d) basis set with the GAMESS software [47]. The electrostatic potential extracted from HF calculations was converted in point charges with the RESP method [48]. HF simulations were also used to validate the classical potential. Almost all Lennard–Jones coefficient and bond/angle/dihedral constants generated from GAFF2 potential satisfactorily agreed with the HF calculations. However, in one case, the C–CO_2^- bond of DF, we had to remodel the potential substituting the typical harmonic bond potential used in GAFF2 with a reparametrized Morse potential, better representative of the energy profile obtained with the HF simulations as already done in literature for similar C–CO_2^- bonds [49]. Additional details can be found in the supporting information.

Data availability statement

The data that support the findings of this study are available upon reasonable request from the authors.

Acknowledgments

This work is part of the 'DESAL' project funded by Politecnico di Torino through the call 'Bando dei Talenti'.

Author contributions

The manuscript was written through contributions of all authors. All authors have given approval to the final version of the manuscript. The authors declare no competing interests.

ORCID iDs

Federico Raffone https://orcid.org/0000-0001-5045-7533
Giancarlo Cicero https://orcid.org/0000-0002-2920-9882

References

[1] Kumar P, Sharma N, Ranjan R, Kumar S, Bhat Z F and Jeong D K 2013 Perspective of membrane technology in dairy industry: a review *Asian-Australas. J. Anim. Sci.* **26** 1347
[2] Nicolaisen B 2003 Developments in membrane technology for water treatment *Desalination* **153** 355–60
[3] Curcio E, Di Profio G, Fontananova E and Drioli E 2015 Membrane technologies for seawater desalination and brackish water treatment *Advances in Membrane Technologies for Water Treatment* (Elsevier) pp 411–41
[4] Lezzoche A, Aixalà-Perelló A, Pedico A, Laurenti M, Raffone F and Lamberti A 2023 Water flow-induced energy harvesting exploiting stacked graphene oxide membranes *Adv. Sustain. Syst.* 2300046
[5] Peyravi M, Jahanshahi M and Banafti S 2020 Application of membrane technology in beverage production and safety *Safety Issues in Beverage Production* (Elsevier) pp 271–308
[6] Warsinger D M *et al* 2018 A review of polymeric membranes and processes for potable water reuse *Prog. Polym. Sci.* **81** 209–37
[7] Castro C *et al* 2018 Graphene-based membrane technology: reaching out to the oil and gas industry *Geofluids* **2018** 1–13
[8] Jiang Y, Biswas P and Fortner J D 2016 A review of recent developments in graphene-enabled membranes for water treatment *Environ. Sci. Water Res. Technol.* **2** 915–22
[9] Yi M and Shen Z 2015 A review on mechanical exfoliation for the scalable production of graphene *J. Mater. Chem.* A **3** 11700–15
[10] Yang W *et al* 2013 Epitaxial growth of single-domain graphene on hexagonal boron nitride *Nat. Mater.* **12** 792–7
[11] Zhang Y I, Zhang L and Zhou C 2013 Review of chemical vapor deposition of graphene and related applications *Acc. Chem. Res.* **46** 2329–39
[12] Cohen-Tanugi D and Grossman J C 2012 Water desalination across nanoporous graphene *Nano Lett.* **12** 3602–8
[13] Cohen-Tanugi D and Grossman J C 2014 Mechanical strength of nanoporous graphene as a desalination membrane *Nano Lett.* **14** 6171–8
[14] Leenaerts O, Partoens B and Peeters F M 2009 Water on graphene: hydrophobicity and dipole moment using density functional theory *Phys. Rev.* B **79** 235440
[15] Kozbial A, Zhou F, Li Z, Liu H and Li L 2016 Are graphitic surfaces hydrophobic? *Acc. Chem. Res.* **49** 2765–73
[16] Zhang W, Zhang Y, Wang Y, Tian S, Han N, Li W, Wang W, Liu H, Yan X and Zhang X 2022 Fluffy-like amphiphilic graphene oxide (f-GO) and its effects on improving the antifouling of PAN-based composite membranes *Desalination* **527** 115575
[17] O'Hern S C, Stewart C A, Boutilier M S H, Idrobo J-C, Bhaviripudi S, Das S K, Kong J, Laoui T, Atieh M and Karnik R 2012 Selective molecular transport through intrinsic defects in a single layer of CVD graphene *ACS Nano* **6** 10130–8
[18] Kafiah F M, Khan Z, Ibrahim A, Karnik R, Atieh M and Laoui T 2016 Monolayer graphene transfer onto polypropylene and polyvinylidenedifluoride microfiltration membranes for water desalination *Desalination* **388** 29–37
[19] Kazemi A S, Hosseini S M and Abdi Y 2019 Large total area membrane of suspended single layer graphene for water desalination *Desalination* **451** 160–71
[20] Kazemi A S, Abdi Y, Eslami J and Das R 2019 Support based novel single layer nanoporous graphene membrane for efficacious water desalination *Desalination* **451** 148–59
[21] Surwade S P, Smirnov S N, Vlassiouk I V, Unocic R R, Veith G M, Dai S and Mahurin S M 2015 Water desalination using nanoporous single-layer graphene *Nat. Nanotechnol.* **10** 459–64
[22] Agrawal K V *et al* 2017 Fabrication, pressure testing, and nanopore formation of single-layer graphene membranes *J. Phys. Chem.* C **121** 14312–21
[23] O'Hern S C, Boutilier M S H, Idrobo J-C, Song Y, Kong J, Laoui T, Atieh M and Karnik R 2014 Selective ionic transport through tunable subnanometer pores in single-layer graphene membranes *Nano Lett.* **14** 1234–41
[24] Anand A, Unnikrishnan B, Mao J Y, Lin H J and Huang C C 2018 Graphene-based nanofiltration membranes for improving salt rejection, water flux and antifouling–a review *Desalination* **429** 119–33
[25] Joshi R K, Alwarappan S, Yoshimura M, Sahajwalla V and Nishina Y 2015 Graphene oxide: the new membrane material *Appl. Mater. Today* **1** 1–12
[26] Raffone F, Savazzi F and Cicero G 2019 Controlled pore generation in single-layer graphene oxide for membrane desalination *J. Phys. Chem. Lett.* **10** 7492–7
[27] Raffone F, Savazzi F and Cicero G 2021 Molecular dynamics study of the pore formation in single layer graphene oxide by a thermal reduction process *Phys. Chem. Chem. Phys.* **23** 11831–6
[28] Subramani A and Jacangelo J G 2015 Emerging desalination technologies for water treatment: a critical review *Water Res.* **75** 164–87
[29] Choi K, Droudian A, Wyss R M, Schlichting K-P and Park H G 2018 Multifunctional wafer-scale graphene membranes for fast ultrafiltration and high permeation gas separation *Sci. Adv.* **4** 1–11
[30] Deng S and Berry V 2016 Wrinkled, rippled and crumpled graphene: an overview of formation mechanism, electronic properties, and applications *Mater. Today* **19** 197–212
[31] Lee H C, Liu -W-W, Chai S-P, Mohamed A R, Aziz A, Khe C-S, Hidayah N S and Hashim U 2017 Review of the synthesis, transfer, characterization and growth mechanisms of single and multilayer graphene *RSC Adv.* **7** 15644–93
[32] Seo D H *et al* 2018 Anti-fouling graphene-based membranes for effective water desalination *Nat. Commun.* **9** 1–12
[33] Meyer J C *et al* 2012 Accurate measurement of electron beam induced displacement cross sections for single-layer graphene *Phys. Rev. Lett.* **108** 196102
[34] Kotakoski J, Santos-Cottin D and Krasheninnikov A V 2012 Stability of graphene edges under electron beam: equilibrium energetics versus dynamic effects *ACS Nano* **6** 671–6
[35] Seidel C, Kopf H, Gotsmann B, Vieth T, Fuchs H and Reihs K 1999 Ar plasma treated and Al metallised polycarbonate: a XPS, mass spectroscopy and SFM study *Appl. Surf. Sci.* **150** 19–33
[36] Xu M, Fujita D, Gao J and Hanagata N 2010 Auger electron spectroscopy: a rational method for determining thickness of graphene films *ACS Nano* **4** 2937–45
[37] Lourenço M A O, Fontana M, Jagdale P, Pirri C F and Bocchini S 2021 Improved CO_2 adsorption properties through amine functionalization of multi-walled carbon nanotubes *Chem. Eng. J.* **414** 128763
[38] Barinov A, Malcioglu O B, Fabris S, Sun T, Gregoratti L, Dalmiglio M and Kiskinova M 2009 Initial stages of oxidation on graphitic surfaces: photoemission study and density functional theory calculations *J. Phys. Chem.* C **113** 9009–13
[39] Barinov A, Üstünel H, Fabris S, Gregoratti L, Aballe L, Dudin P, Baroni S and Kiskinova M 2007 Defect-controlled transport properties of metallic atoms along carbon nanotube surfaces *Phys. Rev. Lett.* **99** 46803
[40] Risplendi F, Raffone F, Lin L C, Grossman J C and Cicero G 2020 fundamental insights on hydration environment of

boric acid and its role in separation from saline water *J. Phys. Chem.* C **124** 1438–45
[41] Cheng P, Moehring N K, Idrobo J C, Ivanov I N and Kidambi P R 2021 Scalable synthesis of nanoporous atomically thin graphene membranes for dialysis and molecular separations: via facile isopropanol-assisted hot lamination *Nanoscale* **13** 2825–37
[42] Tougaard S 2021 Practical guide to the use of backgrounds in quantitative XPS *J. Vac. Sci. Technol.* A **39** 11201
[43] Plimpton S 1995 Fast parallel algorithms for short-range molecular dynamics *J. Comput. Phys.* **117** 1–19
[44] Thompson A P *et al* 2022 LAMMPS—a flexible simulation tool for particle-based materials modeling at the atomic, meso, and continuum scales *Comput. Phys. Commun.* **271** 108171
[45] Jorgensen W L, Chandrasekhar J, Madura J D, Impey R W and Klein M L 1983 Comparison of simple potential functions for simulating liquid water *J. Chem. Phys.* **79** 926–35
[46] Wang J, Wolf R M, Caldwell J W, Kollman P A and Case D A 2004 Development and testing of a general Amber force field *J. Comput. Chem.* **25** 1157–74
[47] Barca G M J *et al* 2020 Recent developments in the general atomic and molecular electronic structure system *J. Chem. Phys.* **152** 154102
[48] Bayly C I, Cieplak P, Cornell W D and Kollman P A 1993 A well-behaved electrostatic potential based method using charge restraints for deriving atomic charges: the RESP model *J. Phys. Chem.* **97** 10269–80
[49] Raffone F, Lamberti A and Cicero G 2023 Tuning the potential drop at graphene/protic ionic liquid interface by molecular structure engineering *Electrochim. Acta* **458** 142344